CONDENSED MATTER PHYSICS

Colossal anomalous Nernst effect in a correlated noncentrosymmetric kagome ferromagnet

T. Asaba[1]*, V. Ivanov[2], S. M. Thomas[1], S. Y. Savrasov[2], J. D. Thompson[1], E. D. Bauer[1], F. Ronning[3]*

The transverse voltage generated by a temperature gradient in a perpendicularly applied magnetic field, termed the Nernst effect, has promise for thermoelectric applications and for probing electronic structure. In magnetic materials, an anomalous Nernst effect (ANE) is possible in a zero magnetic field. We report a colossal ANE in the ferromagnetic metal $UCo_{0.8}Ru_{0.2}Al$, reaching 23 microvolts per kelvin. Uranium's 5*f* electrons provide strong electronic correlations that lead to narrow bands, a known route to producing a large thermoelectric response. In addition, uranium's strong spin-orbit coupling produces an intrinsic transverse response in this material due to the Berry curvature associated with the relativistic electronic structure. Theoretical calculations show that in $UCo_{0.8}Ru_{0.2}Al$ at least 148 Weyl nodes, and two nodal lines, exist within 60 millielectron volt of the Fermi level. This work demonstrates that magnetic actinide materials can host strong Nernst and Hall responses due to their combined correlated and topological nature.

INTRODUCTION

Because electrons carry both heat and charge, the transport of one is necessarily related to the other. Thermoelectric applications aim to exploit this fact by converting heat or charge flow into electric voltages or temperature gradients (*1*, *2*). In the presence of a magnetic field, transverse responses are possible. It has been argued that the transverse geometry allows one to convert heat into electrical energy much more efficiently than the conventional longitudinal geometry (*1*, *3*, *4*). In conventional materials, however, the amplitude of the transverse anomalous Nernst effect (ANE) has been too small to realize practical thermoelectric devices.

Recently, it has been recognized that the Berry curvature associated with the Bloch waves of electrons generates an additional and potentially very large transverse response in magnetic materials (*5*–*9*). This is exemplified by the full-Heusler ferromagnet Co_2MnGa whose ANE at room temperature is 6 μV/K and reaches to a record 8 μV/K at T = 400 K (*3*). This value is larger than typical ferromagnets, and theoretical calculations reveal that the large ANE is a consequence of the intrinsic Berry curvature contribution. After the triumph of Co_2MnGa, a natural question arises: Can one further enhance or maximize the size of the ANE for applications or due to fundamental constraints? Here, we examine a uranium compound, which has multiple favorable attributes for enhancing the Berry curvature and ANE, and we find an ANE, which is even four times larger than found in Co_2MnGa.

The Nernst Effect is related to the thermoelectric ($\bar{\alpha}$) and conductivity ($\bar{\sigma}$) tensors through the expression $S_{xy} = -E_y/\nabla_x T = (\sigma_{xx}\alpha_{xy} - \sigma_{xy}\alpha_{xx})/(\sigma_{xx}^2 + \sigma_{xy}^2)$. The transverse contribution to the thermoelectric and conductivity tensors is directly connected to the Berry curvature Ω_B through

$$\sigma_{xy} = -\frac{e^2}{\hbar}\int_{BZ}\frac{d^3k}{(2\pi)^3} f(k)\,\Omega_B(k) \quad (1)$$

$$\alpha_{xy} = \frac{ek_B}{\hbar}\int_{BZ}\frac{d^3k}{(2\pi)^3} s(k)\,\Omega_B(k) \quad (2)$$

where k_B is the Boltzmann's constant, e is the charge of an electron, ħ is the Planck's constant h divided by 2π, $f(k)$ is the Fermi-Dirac distribution function, $s(k) = -f(k)\ln(f(k)) - (1-f(k))\ln(1-f(k))$, and $\int_{BZ}$ is the integration over the Brillouin zone. At low temperatures, these two quantities are related through the Mott formula (*10*, *11*).

An examination of these equations reveals that large Berry curvatures and small Fermi energies E_F will generate large Hall and Nernst effects, in general. As elaborated on below, to enhance the Berry curvature contribution to the ANE and anomalous Hall effect (AHE), we therefore look for a system with the following properties: (i) a large spin-orbit coupling (SOC), (ii) strong electronic correlations, (iii) ferromagnetic order, and (iv) a kagome lattice structure.

The Berry curvature depends strongly on the SOC. Increasing the strength of the SOC increases the potential occurrence of band inversions, which generate regions of potentially diverging Berry curvature in the Brillouin zone. Depending on the symmetry of the inverted bands, nodal lines and/or Dirac or Weyl nodes may appear. In general, the strength of the SOC increases with increasing atomic number, and hence, we look for materials near the bottom of the periodic table.

To maximize the effects of larger SOC requires multiple bands to reside in the vicinity of the Fermi energy. This can be accomplished through strong electronic correlations, which will shift multiple band crossing points closer to the Fermi energy, thereby enhancing the Berry curvature. Furthermore, the renormalized band structures due to electronic correlations lead to smaller effective Fermi energies, which is known to promote large Seebeck and Nernst responses (*12*, *13*). The need for both strong correlations and large SOC leads us naturally to heavy fermion systems composed of 4*f* and 5*f* elements.

Without broken time-reversal symmetry, a transverse Hall or Nernst response is identically zero. Hence, in the absence of an applied magnetic field, magnetic order is required for a finite ANE or AHE. Although possible in a system with antiferromagnetic order (*8*, *9*, *14*, *15*), the requisite absence of symmetries is guaranteed in a ferromagnetic system.

[1]Materials Physics and Applications Division, Los Alamos National Laboratory, NM, 87545 USA. [2]Department of Physics, University of California, Davis, CA 95616, USA. [3]Institute for Materials Science, Los Alamos National Laboratory, NM, 87545 USA. *Corresponding author. Email: fronning@lanl.gov (F.R.); tasaba@umich.edu (T.A.)

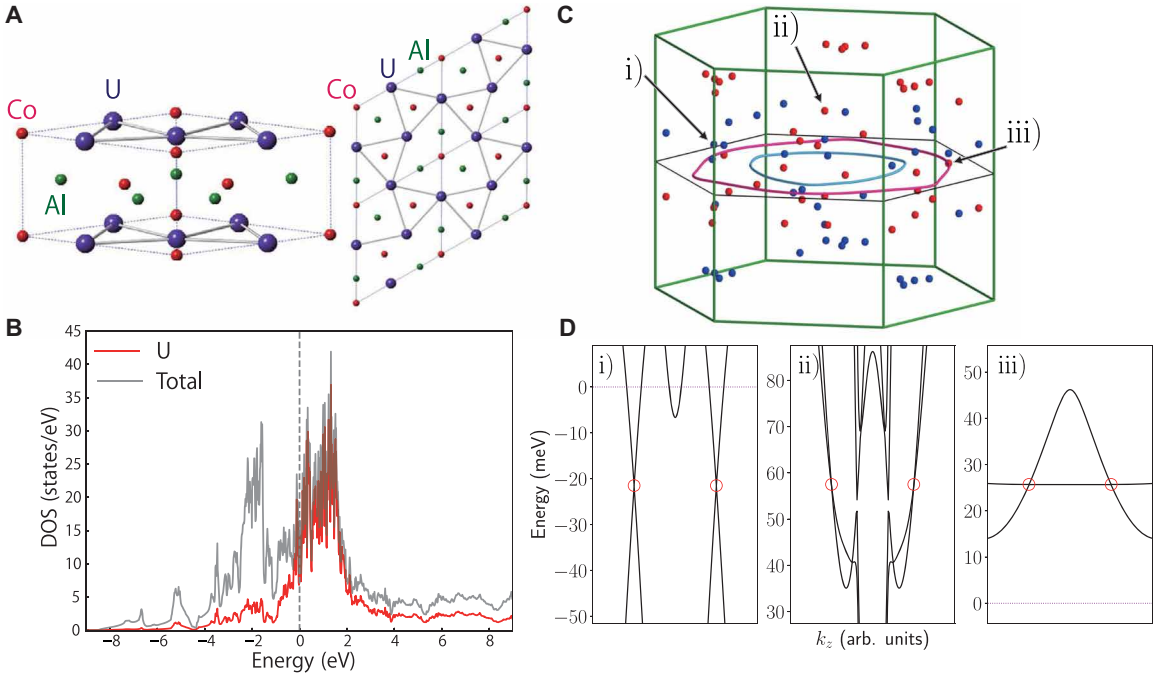

Fig. 1. Crystal structure and theoretical calculations of $UCo_{0.8}Ru_{0.2}Al$. (**A**) Crystal structure of $UCo_{1-x}Ru_xAl$. Left: The unit cell of UCoAl viewed from the [111] direction. A Co atom is replaced by a Ru atom upon doping. Right: The top view of UCoAl. The solid bonds indicate the tilted kagome layer formed by uranium atoms. (**B**) Density of states (DOS) including partial DOS for $UCo_{0.8}Ru_{0.2}Al$. (**C**) Nodal lines and Weyl points within ±60 meV of the Fermi energy in $UCo_{0.8}Ru_{0.2}Al$. For clarity, Weyl pairs with a k_z separation < 0.2 2π/*c* are not shown. (**D**) Band plots for examples of (i) type I, (ii) type II, and (iii) critically tilted Weyl points (red circles), identified with arrows in (C), plotted on the interval $-2k_W < k_z < 2k_W$, where $2k_W$ is the Weyl pair separation along the k_z direction.

In a system with antiferromagnetic interactions, magnetic frustration present in a kagome lattice can lead to additional band renormalization. Although magnetic frustration is presumably absent in a ferromagnetic material, the unrenormalized hopping on a kagome lattice coincidentally produces one flat band. Perhaps this explains, in part, why large AHE and ANE responses have been recently observed in a number of kagome compounds (*6*, *16*–*19*).

In our exploration of materials, we found that the layered distorted kagome lattice system $UCo_{1-x}Ru_xAl$ in the ZrNiAl structure type (shown in Fig. 1A) satisfies all the above criteria. In addition, the crystal structure is noncentrosymmetric, which can generate pairs of Weyl nodes with opposite chiralities. By themselves, such Weyl nodes do not contribute to the AHE and ANE, but they can be further split by the magnetic order. Both parent compounds UCoAl and URuAl are paramagnetic, but much of their solid solution $UCo_{1-x}Ru_xAl$ is ferromagnetic (*20*, *21*). Members of the entire alloy series show relatively large Sommerfeld coefficients γ of ~50 mJ/mol K^2 (*21*–*24*), indicating that charge carriers are moderately heavy. Magnetic x-ray and photoemission measurements also certify the presence of electronic correlations (*25*, *26*). Furthermore, previous work has shown substantial anomalous Hall conductivity (AHC) for dopings close to the quantum-phase transition (*21*). Here, we examine $x = 0.2$ with a critical temperature (T_c) of 56 K, close to the optimal value in the series.

RESULTS

Our spin-polarized theoretical calculations including SOC support our initial conjecture. A partial density of states of $UCo_{0.8}Ru_{0.2}Al$ shown in Fig. 1B reveals a narrow band of uranium *f*-states dominating the electronic structure near E_F. Electronic correlations are expected to further reduce this bandwidth (*24*). The magnitude of the calculated AHC due to the Berry curvature is found to be ~2000 $ohm^{-1}cm^{-1}$, although the value as well as sign, is highly sensitive to details of the electronic structure (*24*). The origin of this large AHC is due to the dominant flat 5*f* uranium bands creating a remarkable number of topological features close to E_F. Figure 1C shows the location of a subset of the Weyl nodes in the Brillouin zone that are within ±60 meV of the Fermi level. There are at least 148 Weyl points, which is, by far, larger than other Weyl materials. There exist both type I and type II Weyl nodes, as well as a few that are proximate to a Lifshitz transition between the two types (see Fig. 1D). Such a "quantum-critical" Weyl node was argued to be the origin of the large Nernstresponse in Co_2MnGa (*3*). We additionally find two topological nodal lines close to E_F within the σ_z mirror plane (Fig. 1C). These nodal lines arise at the crossing of bands belonging to distinct irreducible representations of the mirror plane point group and are protected against perturbations by the existence of mirror symmetry. While these nodal lines are substantial sources of Berry curvature, they will not contribute to Ω^z_{xy}. We note that first-principles calculations of the electronic structure of uranium compounds is notoriously challenging, but the main observation of an incredibly large number of Weyl nodes and Berry curvature found here is independent of the details of the electronic structure [see (*24*)].

The temperature dependence of the longitudinal resistivity ρ_{xx} and the Seebeck coefficient S_{xx} of a single crystal of $UCo_{0.8}Ru_{0.2}Al$ is shown in Fig. 2. A kink is observed in both ρ_{xx} and S_{xx} at the ferromagnetic T_c = 56 K. The sample is a bad metal as reflected by the large residual resistivity (105 μ ohm cm). A longitudinal conductivity

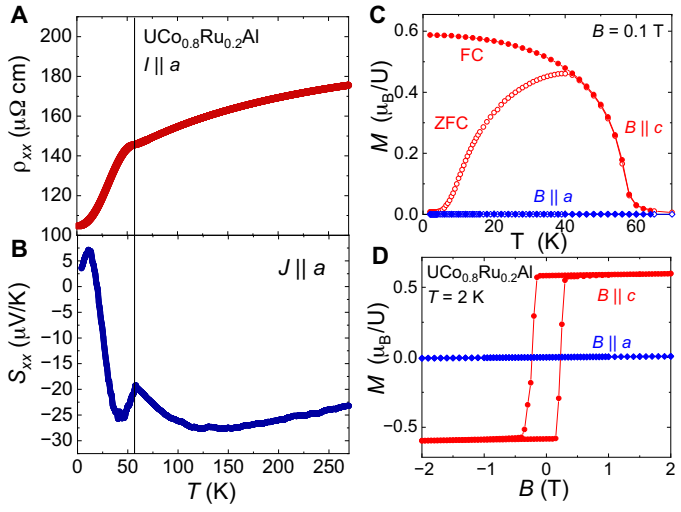

Fig. 2. Longitudinal transport and magnetization properties of single crystalline $UCo_{0.8}Ru_{0.2}Al$. (**A**) Electrical resistivity ρ versus temperature *T* with the current *I* ∥ *a*. The vertical solid line indicates the ferromagnetic critical temperature. (**B**) Seebeck coefficient S_{xx} versus *T* with the heat current *J* ∥ *a*. (**C**) Temperature dependence of the field-cooled (FC) and zero-field-cooled (ZFC) magnetization *M* per formula unit for *B* ∥ *c* (red) and *B* ∥ *a* (blue) in an applied field *B* = 0.1 T. (**D**) Field dependence of the magnetization *M*(*H*) at *T* = 2 K.

σ_{xx} of ~9500 $ohm^{-1}cm^{-1}$, which falls within the moderately dirty regime where $\sigma_{xx} = 3 \times 10^3 - 5 \times 10^5$ $ohm^{-1}cm^{-1}$, is the first indication that the transverse transport will be dominated by the intrinsic contribution (*27*). In the $T = 0$ limit, the S_{xx}/T gives a value of 0.9 μV/K^2. This suggests a Fermi temperature of ~470 K (*12*), consistent with a Fermi temperature of 930 K estimated by specific heat (*24*). We also note that the ratio of the experimental Sommerfeld coefficient to the computed value based on density functional theory implies a mass renormalization of ~3 (*24*).

The temperature- and field-dependent magnetization of $UCo_{0.8}Ru_{0.2}Al$ is shown in Fig. 2. The system shows very strong Ising-type magnetic anisotropy, with the easy axis along the *c* axis. The saturation magnetic moment of 0.59 μ_B/U is consistent with a previous study (*20*) and implies that the uranium 5*f* electrons are rather strongly hybridized with ligand electrons. A small field of $B = 0.1$ T is enough to polarize the magnetic moments during field cooling (FC). Thus, we take the transverse responses (Hall, Nernst, and Righi-Leduc effects) with FC and $B = 0.1$ T conditions, which is small enough to render the ordinary contributions as negligible.

The field and temperature dependence of the Hall, Nernst, and Righi-Leduc effects are shown in Fig. 3. For the field dependence, they all show a step-like behavior similar to the magnetization. The saturated response at high fields in the ordered state confirms that the transverse effects are dominated by the anomalous contribution, and the ordinary component is negligibly small. Consequently, the transverse response discussed in the remainder of the paper implicitly refers to the anomalous component. The vanishing transverse response as the temperature exceeds T_c is also consistent with this picture.

The anomalous Hall effect of $UCo_{0.8}Ru_{0.2}Al$ is found to be very large, as shown in Fig. 3 (A and B). At $T = 40$ K, ρ_{xy} is −16 μ ohm cm, which decreases to −11 μ ohm cm at $T = 2$ K, corresponding to a conductivity of $\sigma_{xy} = 980$ ohm^{-1} cm^{-1}. These values are similar to that of Co_2MnGa and $Co_3Sn_2S_2$ and among the largest values for ferromagnetic metals (*3*, *16*).

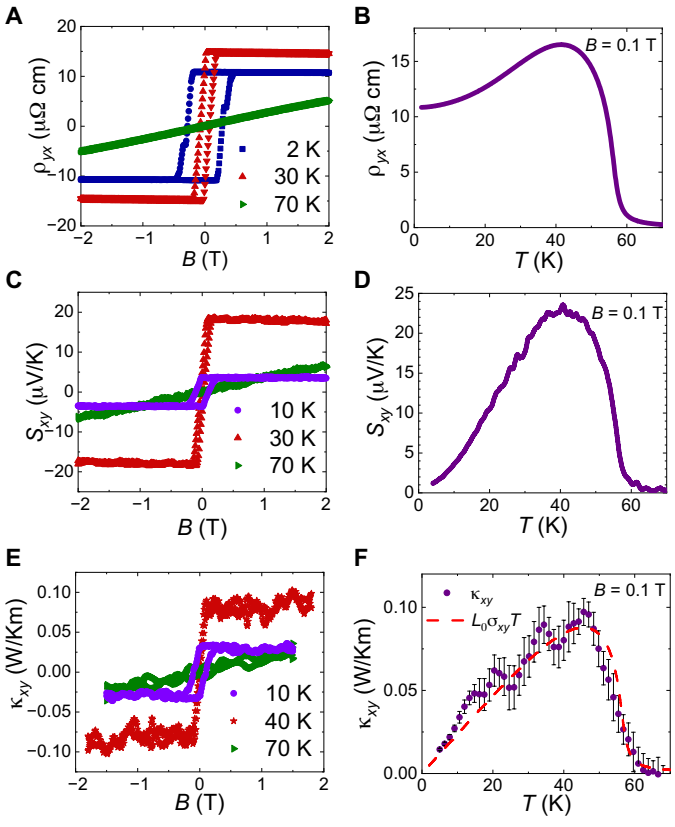

Fig. 3. Colossal anomalous transverse responses from $UCo_{0.8}Ru_{0.2}Al$ with *B* ∥ *c*. (**A** and **B**) Hall effect ρ_{xy} as a function of magnetic field *B* and temperature *T*, respectively. (**C** and **D**) Nernst effect S_{xy} as a function of *B* and *T*, respectively. (**E** and **F**) Thermal Hall (Righi-Leduc) effect κ_{xy} as a function of *B* and *T*, respectively. The red dashed line in (F) is the expected thermal Hall conductivity based on the electrical Hall conductivity if the Wiedemann-Franz law is satisfied. All temperature-dependent data were taken with $B = 0.1$ T.

Next, we display our primary result, a colossal ANE. While the anomalous Hall resistivity is as large as in Co_2MnGa and $Co_3Sn_2S_2$, more unexpectedly, the ANE is found to be colossal in $UCo_{0.8}Ru_{0.2}Al$, reaching 23 μV/K at $T = 40$ K (Fig. 3, C and D). To the best of our knowledge, this is approximately three to four times larger than the current record value of 6 to 8 μV/K held by Co_2MnGa (*3*). Furthermore, in $UCo_{0.8}Ru_{0.2}Al$, the magnitude of S_{xy} at 40 K is comparable to the Seebeck coefficient. Consequently, the anomalous Nernst angle $\tan(\theta_N) = |S_{xy}/S_{xx}|$ reaches 0.92 at 41 K, where both S_{xx} and S_{xy} have extrema with values of −25.5 and 23.5 μV/K, respectively.

Figure 3 (E and F) displays the anomalous thermal Hall conductivity κ_{xy} of $UCo_{0.8}Ru_{0.2}Al$ as a function of field and temperature. To check the validity of the anomalous Wiedemann-Franz (WF) law $L_0 = \frac{\kappa_{xy}}{\sigma_{xy}T}$ where $L_0 = \frac{\pi^2 k_B^2}{3e^2} = 2.44 \times 10^{-8}$ W ohm/K^2, we compared κ_{xy} with $L_0\sigma_{xy}T$ (Fig. 3F). We find that they overlap each other very well, and thus, the WF law is valid. The validity of a transverse WF law indicates that the anomalous transverse entropy and charge flow are governed by the intrinsic contribution from the Berry curvature (*8*, *15*).

DISCUSSION

The AHC as a function of T/T_c for a variety of materials with large transverse responses in heat and charge (*15*, *28*–*30*) is shown in

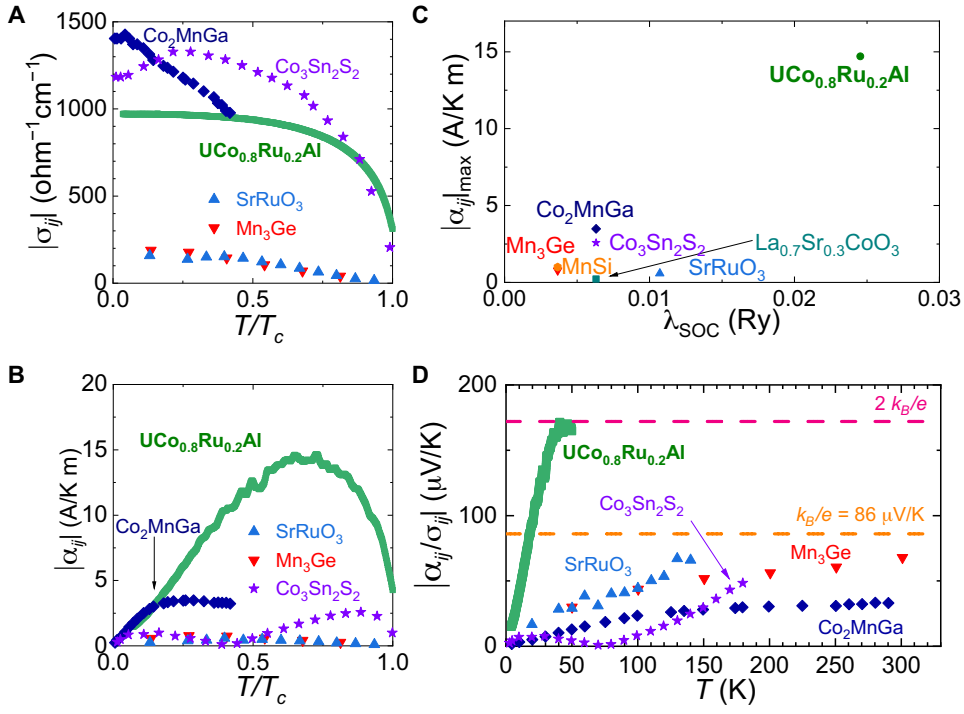

Fig. 4. Anomalous Hall and Peltier conductivity of various magnets. (**A**) AHC σ_{ij} and (**B**) anomalous Peltier conductivity α_{ij} as a function of normalized temperature T/T_c (green line). For comparison, other materials with large anomalous contributions are also shown. (**C**) The maximum value of α_{ij} for various compounds compared with the strength of the SOC of the magnetic element (*31*). The compounds include $UCo_{0.8}Ru_{0.2}Al$ (this work, green circle), Co_2MnGa (blue diamond) (*28*), $Co_3Sn_2S_2$ (purple star) (*30*), $SrRuO_3$ (*29*) (cyan upper triangle), $La_{0.7}Sr_{0.3}CoO_3$ (light green square) (*29*), Mn_3Ge (red lower triangle) (*15*), and MnSi (orange hexagon) (*49*). (**D**) Plot of α_{ij}/σ_{ij} versus T. Orange and pink dashed lines indicate k_B/e and 2 k_B/e, respectively.

Fig. 4A. The AHC of $UCo_{0.8}Ru_{0.2}Al$ is almost temperature-independent below $T = 0.5\ T_c$. This implies that the AHC is independent of scattering rate, which is an additional support that the intrinsic contribution dominates the transverse response in this system. At $T = 2$ K, $|\sigma_{xy}|$ reaches 980 ohm^{-1} cm^{-1} in $UCo_{0.8}Ru_{0.2}Al$, which is comparable to Co_2MnGa, one of the largest intrinsic AHC known. The AHC from $SrRuO_3$ and Mn_3Ge is almost one order of magnitude smaller than that of $UCo_{0.8}Ru_{0.2}Al$. The anomalous Peltier conductivity α_{xy} as a function of T/T_c for these materials is shown in Fig. 4B. The Peltier coefficient is the sum of two contributions $\sigma_{xx}S_{xx}$ and $\sigma_{xy}S_{xx}$. In $UCo_{0.8}Ru_{0.2}Al$, $\sigma_{xx}S_{xy} \gg \sigma_{xy}S_{xx}$ (see the Supplementary Materials). In sharp contrast to the fact that σ_{xy} of $UCo_{0.8}Ru_{0.2}Al$ is comparable to that of Co_2MnGa and $Co_3Sn_2S_2$, α_{xy} of $UCo_{0.8}Ru_{0.2}Al$ is roughly three to four times larger than that of Co_2MnGa, the current record holder for α_{xy}, and $Co_3Sn_2S_2$. α_{xy} of $SrRuO_3$ and Mn_3Ge are notably smaller.

Why is α_{ij} so large in $UCo_{0.8}Ru_{0.2}Al$? In Fig. 4C we plot the maximal value of $|\alpha_{ij}|$ versus λ_{SOC} for various compounds. λ_{SOC} is estimated from atomic calculations of the magnetic element (*31*, *32*). Despite this very rough estimate for the strength of the SOC in these materials, Fig. 4C supports our original conjecture that a large SOC increases the possibility for more band inversions, which can create a large Berry curvature contribution to anomalous transverse response functions (*33*).

A large SOC alone, however, is insufficient to explain the remarkable properties of $UCo_{0.8}Ru_{0.2}Al$, because the maximal contribution from any pair of bands to the AHE is e^2/hc, where c is the c-axis lattice constant, and in this limit, one expects a vanishing ANE. Instead, our electronic structure calculations shown in Fig. 1 reveal that there are many bands in the vicinity of the Fermi energy. This is a consequence of the nature of the 5*f* electrons in uranium. Furthermore, electronic correlations will further renormalize the bands leading to smaller effective Fermi energies, which is known to enhance thermoelectric properties (*12*). Notably, the Sommerfeld coefficient of the heat capacity γ is substantially larger for $UCo_{0.8}Ru_{0.2}Al$ (41 mJ/mol K^2) compared to Co_2MnGa (12 mJ/mol K^2) (*3*). Thus, it is the combination of the small effective Fermi energy and the large SOC that leads to multiple topological features within the energy window set by the SOC and that enables the remarkably large values of both σ_{ij} and α_{ij} in $UCo_{0.8}Ru_{0.2}Al$.

It is interesting to ask which specific features of the electronic structure are most responsible for the large ANE in $UCo_{0.8}Ru_{0.2}Al$. $UCo_{0.8}Ru_{0.2}Al$ crystallizes in the nonsymmorphic space group 189. From basic symmetry considerations, this space group has been argued to have a variety of interesting topological features, including Weyl nodes (*34*–*37*), nodal lines (*38*–*41*), and triple points (*42*, *43*). All of these features appear in our electronic structure calculations (*24*). Notably, one set of critically tilted Weyl points lies 25 meV above E_f, corresponding to a doping of $x \sim 0.07$ in the rigid band picture. For this set of Weyl nodes, we compute values of $\sigma_{xy} \sim 1200$ ohm^{-1} cm^{-1} and $\alpha_{xy} \sim 20$ A(K m)$^{-1}$ at that energy, which may be shifted as a consequence of electronic correlations. Another possibility is that electronic correlations pin the Weyl nodes to the chemical potential as has been suggested in some Weyl-Kondo semimetals (*44*). Additional measurements, such as angle-resolved photoemission spectroscopy, will be required to confirm the identity of the most relevant topological features in $UCo_{0.8}Ru_{0.2}Al$.

Last, we consider the relationship between σ_{ij} and α_{ij}. From the Mott relation, which is valid in the $T = 0$ limit, a large α_{ij}/T implies that σ_{ij} can be enhanced by appropriately tuning the chemical potential. As temperature is increased, the relationship between σ_{ij} and α_{ij} is less straight forward. Behnia *et al.* (*28*) have argued, however, that the ratio of α_{ij}/σ_{ij} is bounded by the ratio of natural units $k_B/e = 86\ \mu V/K$, which reflects the fact that the Peltier coefficient represents the transport of entropy, while the Hall coefficient represents the transport of charge. For $UCo_{0.8}Ru_{0.2}Al$, α_{ij}/σ_{ij} reaches 170 μV/K at $T = 47$ K, as shown in Fig. 4D. This supports the notion that multiple bands are simultaneously contributing to the large Nernst response in $UCo_{0.8}Ru_{0.2}Al$.

In conclusion, we have found a colossal ANE in $UCo_{0.8}Ru_{0.2}Al$. The simultaneous presence of strong SOC and electronic correlations drives narrow bands leading to a gigantic Nernst response and presents an exciting blueprint for how to develop magnetic topological metals for thermoelectric applications.

MATERIALS AND METHODS

A single crystal of nominal composition $UCo_{0.8}Ru_{0.2}Al$ was grown by the Czochralski method in a tri-arc furnace. The crystal structure was confirmed to have the P$\bar{6}$2*m* (# 189) space group with the ZrNiAl structure type. Powder and single-crystal diffraction was performed to confirm the crystal structure and the phase purity of the samples. The sample was oriented, and the quality was further checked by the x-ray Laue method with a photosensitive detector in back-scattering geometry. The measured magnetic properties are in good agreement with previous studies, further confirming the sample quality.

Electronic structure calculations were performed using the local spin density approximation, yielding a ferromagnetic ground state, within the framework of the full potential linear muffin tin orbital method with SOC (*45*). This approximation has been previously used to study UCoAl (*25*, *46*) and other uranium compounds in the same structural family (*47*). Experimental lattice constants were used (*48*), and doping dependence was handled using a rigid band approximation.

Weyl points and other topological features were located, and their topology was verified in a single-shot method (*43*). An initial coarse $\boldsymbol{k}$-grid of 30 × 30 × 30 was used to locate candidate sources/sinks of Berry curvature flux, whose positions were iteratively refined by repeating the procedure on 2 × 2 × 2 grids within each $\boldsymbol{k}$-cube. Additional details can be found in (*24*).

Transport, thermoelectric, and thermal transport measurements were performed in the same setup. A temperature gradient was generated by a 10-kilohm chip resistor attached to one end of the sample and measured by homemade thermocouples with the calibrated table made of Fe-doped gold and chromel. The other end of the sample was attached to a sapphire substrate that was physically clamped to an oxygen-free copper cold finger. Conventional steady-state measurements were performed to measure the thermoelectic power and thermal conductivity. The heating power was carefully monitored so that the thermal and thermoelectric responses were linear with the heating power.

SUPPLEMENTARY MATERIALS

Supplementary material for this article is available at http://advances.sciencemag.org/cgi/content/full/7/13/eabf1467/DC1

REFERENCES AND NOTES

1. L. E. Bell, Cooling, heating, generating power, and recovering waste heat with thermoelectric systems. *Science* **321**, 1457–1461 (2008).
2. J. He, T. M. Tritt, Advances in thermoelectric materials research: Looking back and moving forward. *Science* **357**, eaak9997 (2017).
3. A. Sakai, Y. P. Mizuta, A. A. Nugroho, R. Sihombing, T. Koretsune, M.-T. Suzuki, N. Takemori, R. Ishii, D. Nishio-Hamane, R. Arita, P. Goswami, S. Nakatsuji, Giant anomalous Nernst effect and quantum-critical scaling in a ferromagnetic semimetal. *Nat. Phys.* **14**, 1119–1124 (2018).
4. Y. Sakuraba, K. Hasegawa, M. Mizuguchi, T. Kubota, S. Mizukami, T. Miyazaki, K. Takanashi, Anomalous Nernst effect in $L1_0$-FePt/MnGa thermopiles for new thermoelectric applications. *Appl. Phys. Express* **6**, 033003 (2013).
5. N. Nagaosa, J. Sinova, S. Onoda, A. H. MacDonald, N. P. Ong, Anomalous hall effect. *Rev. Mod. Phys.* **82**, 1539–1592 (2010).
6. S. Nakatsuji, N. Kiyohara, T. Higo, Large anomalous Hall effect in a non-collinear antiferromagnet at room temperature. *Nature* **527**, 212–215 (2015).
7. A. K. Nayak, J. E. Fischer, Y. Sun, B. Yan, J. Karel, A. C. Komarek, C. Shekhar, N. Kumar, W. Schnelle, J. Kübler, C. Felser, S. S. P. Parkin, Large anomalous Hall effect driven by a nonvanishing Berry curvature in the noncolinear antiferromagnet Mn_3Ge. *Sci. Adv.* **2**, e1501870 (2016).
8. X. Li, L. Xu, L. Ding, J. Wang, M. Shen, X. Lu, Z. Zhu, K. Behnia, Anomalous Nernst and Righi-Leduc effects in Mn_3Sn: Berry curvature and entropy flow. *Phys. Rev. Lett.* **119**, 056601 (2017).
9. M. Ikhlas, T. Tomita, T. Koretsune, M.-T. Suzuki, D. Nishio-Hamane, R. Arita, Y. Otani, S. Nakatsuji, Large anomalous Nernst effect at room temperature in a chiral antiferromagnet. *Nat. Phys.* **13**, 1085–1090 (2017).
10. M. Cutler, N. F. Mott, Observation of Anderson localization in an electron gas. *Phys. Rev.* **181**, 1336–1340 (1969).
11. D. Xiao, Y. Yao, Z. Fang, Q. Niu, Berry-phase effect in anomalous thermoelectric transport. *Phys. Rev. Lett.* **97**, 026603 (2006).
12. K. Behnia, D. Jaccard, J. Flouquet, On the thermoelectricity of correlated electrons in the zero-temperature limit. *J. Phys. Condens. Matter* **16**, 5187 (2004).
13. K. Behnia, H. Aubin, Nernst effect in metals and superconductors: A review of concepts and experiments. *Rep. Prog. Phys.* **79**, 046502 (2016).
14. C. Wuttke, F. Caglieris, S. Sykora, F. Scaravaggi, A. U. Wolter, K. Manna, V. Süss, C. Shekhar, C. Felser, B. Büchner, C. Hess, Berry curvature unravelled by the anomalous Nernst effect in Mn_3Ge. *Phys. Rev. B* **100**, 085111 (2019).
15. L. Xu, X. Li, X. Lu, C. Collignon, H. Fu, J. Koo, B. Fauqué, B. Yan, Z. Zhu, K. Behnia, Finite-temperature violation of the anomalous transverse Wiedemann-Franz law. *Sci. Adv.* **6**, eaaz3522 (2020).
16. E. Liu, Y. Sun, N. Kumar, L. Muechler, A. Sun, L. Jiao, S.-Y. Yang, D. Liu, A. Liang, Q. Xu, J. Kroder, V. Süß, H. Borrmann, C. Shekhar, Z. Wang, C. Xi, W. Wang, W. Schnelle, S. Wirth, Y. Chen, S. T. B. Goennenwein, C. Felser, Giant anomalous Hall effect in a ferromagnetic kagome-lattice semimetal. *Nat. Phys.* **14**, 1125–1131 (2018).
17. T. Kida, L. Fenner, A. Dee, I. Terasaki, M. Hagiwara, A. Wills, The giant anomalous Hall effect in the ferromagnet Fe_3Sn_2—a frustrated kagome metal. *J. Phys. Condens. Matter* **23**, 112205 (2011).
18. L. Ye, M. Kang, J. Liu, F. von Cube, C. R. Wicker, T. Suzuki, C. Jozwiak, A. Bostwick, E. Rotenberg, D. C. Bell, L. Fu, R. Comin, J. G. Checkelsky, Massive Dirac fermions in a ferromagnetic kagome metal. *Nature* **555**, 638–642 (2018).
19. G. Xu, B. Lian, S.-C. Zhang, Intrinsic quantum anomalous hall effect in the kagome lattice $Cs_2LiMn_3F_{12}$. *Phys. Rev. Lett.* **115**, 186802 (2015).
20. A. V. Andreev, L. Havela, V. Sechovsk, M. I. Bartashevich, J. Šebek, R. V. Dremov, I. K. Kozlovskaya, Ferromagnetism in the $UCo_{1-x}Ru_xAl$ quasiternary intermetallics. *Philos. Mag. B* **75**, 827–844 (1997).
21. J. Pospíšil, P. Opletal, M. Vališka, Y. Tokunaga, A. Stunault, Y. Haga, N. Tateiwa, B. Gillon, F. Honda, T. Yamamura, V. Nižňanský, E. Yamamoto, D. Aoki, Properties and Collapse of the Ferromagnetism in $UCo_{1-x}Ru_xAl$ Studied in Single Crystals. *J. Phys. Soc. Jpn.* **85**, 034710 (2016).
22. P. A. Veenhuizen, F. R. De Boer, A. A. Menovsky, V. Sechovsky, L. Havela, Magnetic properties of URuAl and URhAl single crystals. *Le Journal de Physique Colloques* **49**, C8–485 (1988).
23. T. D. Matsuda, H. Sugawara, Y. Aoki, H. Sato, A. V. Andreev, Y. Shiokawa, V. Sechovsky, L. Havela, Transport properties of the anisotropic itinerant-electron metamagnet UCoAl. *Phys. Rev. B* **62**, 13852–13855 (2000).
24. See the Supplementary Materials.
25. V. N. Antonov, B. N. Harmon, O. V. Andryushchenko, L. V. Bekenev, A. N. Yaresko, Electronic structure and x-ray magnetic circular dichroism in uranium compounds. II. U7 Al (*T*= Co, Rh, and Pt) intermetallics. *Phys. Rev. B* **68**, 214425 (2003).
26. S.-i. Fujimori, Y. Takeda, T. Okane, Y. Saitoh, A. Fujimori, H. Yamagami, Y. Haga, E. Yamamoto, Y. Ōnuki, Electronic structures of uranium compounds studied by soft x-ray photoelectron spectroscopy. *J. Phys. Soc. Jpn.* **85**, 062001 (2016).

27. S. Onoda, N. Sugimoto, N. Nagaosa, Quantum transport theory of anomalous electric, thermoelectric, and thermal Hall effects in ferromagnets. *Phys. Rev. B* **77**, 165103 (2008).
28. L. Xu, X. Li, L. Ding, T. Chen, A. Sakai, B. Fauqué, S. Nakatsuji, Z. Zhu, K. Behnia, Anomalous transverse response of Co_2 MnGa and universality of the room-temperature $\alpha_{ij}^A/\sigma_{ij}^A$ ratio across topological magnets. *Phys. Rev. B* **101**, 180404 (2020).
29. T. Miyasato, N. Abe, T. Fujii, A. Asamitsu, S. Onoda, Y. Onose, N. Nagaosa, Y. Tokura, Crossover behavior of the anomalous Hall effect and anomalous Nernst effect in itinerant ferromagnets. *Phys. Rev. Lett.* **99**, 086602 (2007).
30. L. Ding, J. Koo, L. Xu, X. Li, X. Lu, L. Zhao, Q. Wang, Q. Yin, H. Lei, B. Yan, Z. Zhu, K. Behnia, Intrinsic anomalous Nernst effect amplified by disorder in a half-metallic semimetal. *Phys. Rev. X* **9**, 041061 (2019).
31. K. Shanavas, Z. S. Popović, S. Satpathy, Theoretical model for Rashba spin-orbit interaction in *d* electrons. *Phys. Rev. B* **90**, 165108 (2014).
32. F. Herman, S. Skillman, *Atomic Structure Calculations* (Engelwood Cliffs, NJ, 1963).
33. D. Xiao, M.-C. Chang, Q. Niu, Berry phase effects on electronic properties. *Rev. Mod. Phys.* **82**, 1959–2007 (2010).
34. S.-M. Huang, S.-Y. Xu, I. Belopolski, C.-C. Lee, G. Chang, B. Wang, N. Alidoust, G. Bian, M. Neupane, C. Zhang, S. Jia, A. Bansil, H. Lin, M. Z. Hasan, A Weyl Fermion semimetal with surface Fermi arcs in the transition metal monopnictide TaAs class. *Nat. Commun.* **6**, 7373 (2015).
35. A. A. Soluyanov, D. Gresch, Z. Wang, Q. Wu, M. Troyer, X. Dai, B. A. Bernevig, Type-II weyl semimetals. *Nature* **527**, 495–498 (2015).
36. X. Wan, A. M. Turner, A. Vishwanath, S. Y. Savrasov, Topological semimetal and Fermi-arc surface states in the electronic structure of pyrochlore iridates. *Phys. Rev. B* **83**, 205101 (2011).
37. H. Weng, C. Fang, Z. Fang, B. A. Bernevig, X. Dai, Weyl semimetal phase in noncentrosymmetric transition-metal monophosphides. *Phys. Rev. X* **5**, 011029 (2015).
38. A. A. Burkov, M. D. Hook, L. Balents, Topological nodal semimetals. *Phys. Rev. B* **84**, 235126 (2011).
39. Y. Du, F. Tang, D. Wang, L. Sheng, E.-j. Kan, C.-G. Duan, S. Y. Savrasov, X. Wan, CaTe: A new topological node-line and Dirac semimetal. *npj Quantum Mater.* **2**, 3 (2017).
40. Y. Kim, B. J. Wieder, C. L. Kane, A. M. Rappe, Dirac line nodes in inversion-symmetric crystals. *Phys. Rev. Lett.* **115**, 036806 (2015).
41. R. Yu, H. Weng, Z. Fang, X. Dai, X. Hu, Topological node-line semimetal and Dirac semimetal state in antiperovskite Cu_3PdN. *Phys. Rev. Lett.* **115**, 036807 (2015).
42. Z. Zhu, G. W. Winkler, Q. Wu, J. Li, A. A. Soluyanov, Triple point topological metals. *Phys. Rev. X* **6**, 031003 (2016).
43. V. Ivanov, S. Y. Savrasov, Monopole mining method for high-throughput screening for Weyl semimetals. *Phys. Rev. B* **99**, 125124 (2019).
44. H.-H. Lai, S. E. Grefe, S. Paschen, Q. Si, Weyl–kondo semimetal in heavy-fermion systems. *Proc. Natl. Acad. Sci. U.S.A.* **115**, 93–97 (2018).
45. S. Y. Savrasov, Linear-response theory and lattice dynamics: A muffin-tin-orbital approach. *Phys. Rev. B* **54**, 16470–16486 (1996).
46. M. Kučera, J. Kuneš, A. Kolomiets, M. Diviš, A. V. Andreev, V. Sechovskỳ, J.-P. Kappler, A. Rogalev, X-ray magnetic circular dichroism studies of 5 *f* magnetism in UCoAl and UPtAl. *Phys. Rev. B* **66**, 144405 (2002).
47. T. Gasche, S. Auluck, M. S. S. Brooks, B. Johansson, Theory of the magnetism of ternary uranium compounds. *J. Magn. Magn. Mater.* **104–107**, 37–38 (1992).
48. D. J. Lam, J. B. Darby Jr., J. W. Downey, L. J. Norton, Equiatomic ternary compounds of uranium and aluminium with group viii transition elements. *J. Nucl. Mater.* **22**, 22–27 (1967).
49. Y. Hirokane, Y. Tomioka, Y. Imai, A. Maeda, Y. Onose, Longitudinal and transverse thermoelectric transport in MnSi. *Phys. Rev. B* **93**, 014436 (2016).
50. T. Gasche, M. S. S. Brooks, B. Johansson, Ground-state properties of ternary uranium compounds: I. hybridization effects. *J. Phys. Condens. Matter* **7**, 9499 (1995).
51. T. Gasche, M. Brooks, B. Johansson, Ground-state properties of ternary uranium compounds: II. magnetic properties. *J. Phys. Condens. Matter* **7**, 9511 (1995).
52. S. Chang, H. Nakotte, A. Andreev, H. Bordallo, L. Havela, V. Sechovsky, M. Torikachvili, Magnetism in some $UCO_{1/3}$ $T_{2/3}$ Al solid solutions (t= transition metal). *J. Appl. Phys.* **87**, 6812–6814 (2000).
53. S. Chang, H. Nakotte, A. J. Schultz, H. N. Bordallo, M. S. Torikachvili, V. Sechovsky, A. V. Andreev, Crystallographic order and magnetism in $UCO_{1/3}T_{2/3}Al$ compounds (T= Ru, Rh, Pt). *Physica B Condens. Matter* **276–278**, 634–635 (2000).
54. A. V. Andreev, V. Sechovsky, L. Havela, J. Šebek, M. I. Bartashevich, T. Goto, K. Kamishima, D. A. Andreev, V. S. Gaviko, R. V. Dremov, I. K. Kozlovskaya, Onset of ferromagnetism between the paramagnets UCoAl and URuAl. *Czech. J. Phys.* **46**, 3385–3386 (1996).
55. V. Ivanov, X. Wan, S. Y. Savrasov, Correlation driven topological insulator-to-weyl semimetal transition in actinide system UNiSn. arXiv:1809.09543 [cond-mat.str-el] (25 September 2018).
56. A. A. Zyuzin, R. P. Tiwari, Intrinsic anomalous hall effect in type-II weyl semimetals. *JETP Letters* **103**, 717–722 (2016).
57. K. Kadowaki, S. Woods, Universal relationship of the resistivity and specific heat in heavy-fermion compounds. *Solid State Commun.* **58**, 507–509 (1986).

Acknowledgments: We thank P. Rosa and X. Wan for useful discussions. **Funding:** The experimental work was performed at Los Alamos National Laboratory under the auspices of the U.S. Department of Energy, Office of Science, Basic Energy Sciences, Materials Sciences and Engineering Division. Theoretical calculations performed by V.I. and S.Y.S. are supported by NSF DMR grant no. 1832728. T.A. acknowledges support from a LANL LDRD Directors Postdoctoral Fellowship. **Author contributions:** T.A. and F.R. designed the experiment and analyzed the data. T.A., S.M.T., and F.R. built the transport measurement setup. T.A. performed the transport and heat capacity measurements. J.D.T. carried out the magnetic measurements. V.I. and S.Y.S. performed the theoretical calculations. E.D.B. prepared the sample. All authors contributed to writing the manuscript. **Competing interests:** The authors declare that they have no competing interests. **Data and materials availability:** All data needed to evaluate the conclusions in the paper are present in the paper and/or the Supplementary Materials. Additional data related to this paper may be requested from the authors.

Submitted 8 October 2020
Accepted 9 February 2021
Published 26 March 2021
10.1126/sciadv.abf1467

Citation: T. Asaba, V. Ivanov, S. M. Thomas, S. Y. Savrasov, J. D. Thompson, E. D. Bauer, F. Ronning, Colossal anomalous Nernst effect in a correlated noncentrosymmetric kagome ferromagnet. *Sci. Adv.* **7**, eabf1467 (2021).

Science Advances

Colossal anomalous Nernst effect in a correlated noncentrosymmetric kagome ferromagnet

T. Asaba, V. Ivanov, S. M. Thomas, S. Y. Savrasov, J. D. Thompson, E. D. Bauer and F. Ronning

Sci Adv **7** (13), eabf1467.
DOI: 10.1126/sciadv.abf1467